

# G<sup>2</sup>DA: Geometry-Guided Dual-Alignment Learning for RGB-Infrared Person Re-Identification

Lin Wan, Zongyuan Sun, Qianyan Jing, Yehansen Chen, Lijing Lu, and Zhihang Li

**Abstract**—RGB-Infrared (IR) person re-identification aims to retrieve person-of-interest between heterogeneous modalities, suffering from large modality discrepancy caused by different sensory devices. Existing methods mainly focus on global-level modality alignment, whereas neglect sample-level modality divergence to some extent, leading to performance degradation. This paper attempts to find RGB-IR ReID solutions from tackling sample-level modality difference, and presents a Geometry-Guided Dual-Alignment learning framework (G<sup>2</sup>DA), which jointly enhances modality-invariance and reinforces discriminability with human topological structure in features to boost the overall matching performance. Specifically, G<sup>2</sup>DA extracts accurate body part features with a pose estimator, serving as a semantic bridge complementing the missing local details in global descriptor. Based on extracted local and global features, a novel distribution constraint derived from optimal transport is introduced to mitigate the modality gap in a fine-grained sample-level manner. Beyond pair-wise relations across two modalities, it additionally measures the structural similarity of different parts, thus both multi-level features and their relations are kept consistent in the common feature space. Considering the inherent human-topology information, we further advance a geometry-guided graph learning module to refine each part features, where relevant regions can be emphasized while meaningless ones are suppressed, effectively facilitating robust feature learning. Extensive experiments on two standard benchmark datasets validate the superiority of our proposed method, yielding competitive performance over the state-of-the-art approaches.

**Index Terms**—Person re-identification, cross-modality matching, optimal transport, feature alignment, channel exchange.

## I. INTRODUCTION

**P**ERSON re-identification (ReID) refers to a large-scale image retrieval task, aiming to match a specific pedestrian from multiple non-overlapping camera views [1], [2]. It has picked up momentum in computer vision for its great value in video surveillance and security application [3], [4]. Currently, most conventional ReID methods [5]–[9] dedicate to RGB-based cross-view matching task, where all the images are captured by visible cameras in the daytime [10]. However, poor illumination (e.g., at night-time) often significantly deteriorates the recognition performance of visible cameras [11]. Alternatively, The technique of infrared imaging provides an effective and inexpensive way to collect images robust

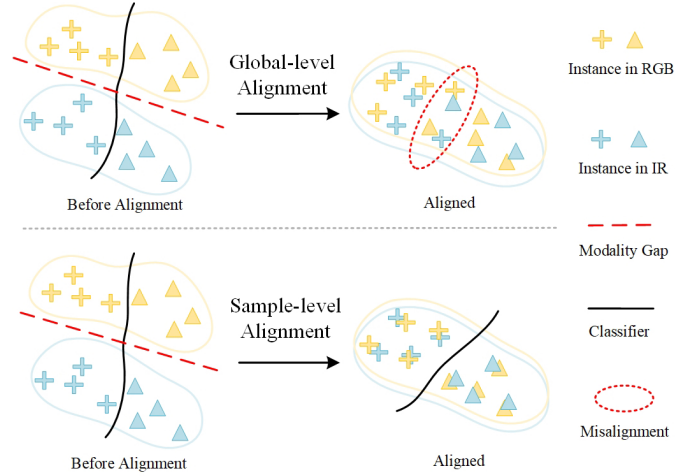


Fig. 1. Comparison of prior works and the proposed method. **Top:** Previous approaches mainly concentrate on global-level modality alignment, possibly leading to misalignment of some instances. **Bottom:** The proposed method aims to achieve fine-grained sample-level alignment by additionally imposing a novel distribution constraint over every paired image. Please refer to the text for more details.

to lighting conditions change [12]. Consequently, matching person images across different sensing mechanisms raises the problem of RGB-Infrared cross-modality person ReID (RGB-IR ReID).

Different from the visible spectrum-based re-identification problem, RGB-IR based person ReID encounters the challenge of extra modality discrepancy brought in by different imaging mechanisms. Specifically, RGB images are captured by visible cameras and store information of three color channels attained from visible light, whilst IR pictures are generated by infrared cameras and have only one channel carrying information from infrared radiation [13], [14]. This intrinsic modality heterogeneity is the main impediment that get in the way of applying most of well-performing single-modality ReID techniques to cross-modality matching tasks [15]. For instance, although playing a critical role in RGB-based re-identification, color information becomes ineffective cues in infrared modality since it is unable to find common visual areas with the same color between RGB and IR images [16]. Moreover, high inter-class similarity and dramatic intra-class variations caused by different illumination conditions, poses, viewpoints and backgrounds, which are also the fundamental challenges in conventional ReID tasks [17], are further exacerbated by the modality gap, leading to more difficulties for image alignment.

Currently, the rapid development of RGB-IR ReID is driven

(Corresponding author: Zhihang Li)

Lin Wan, Zongyuan Sun, Qianyan Jing and Yehansen Chen are with the School of Geography and Information Engineering, China University of Geosciences, Wuhan 430078, China (e-mail: wanlin@cug.edu.cn; sunzongyuan@cug.edu.cn; jingqianyan@cug.edu.cn; chenye Hansen@cug.edu.cn).

Lijing Lu and Zhihang Li are with University of Chinese Academy of Sciences, Beijing 100190, China (e-mail: lulijing2019@ia.ac.cn; zhihang.li@nlpr.ia.ac.cn).

both by deep learning models and the release of large cross-modality ReID datasets (e.g., SYSU-MM01 [18] and RegDB [19]). Existing methods can be roughly grouped into two categories: (1) Adversarial learning-based methods [2], [14], [20], [21]. Some works [2], [20] resort to Generative Adversarial Network (GAN) for domain transfer, i.e., translate the input image into its counterpart modality, thereby eliminating the modality gap in pixel-level. Besides, adversarial learning is also adopted for feature disentanglement. They usually employ adversarial losses to decompose modality-invariant features for modality gap reduction [14] and ID-discriminative features for re-identification [21]. However, adversarial training is unstable and often results in mode collapse [1], [22]. (2) Modality-shared feature learning methods [23]–[30]. These methods seek to learn a shared feature subspace into which RGB and IR images are mapped as modality-invariant features for comparison [31]. Most of them tend to adopt a partially shared CNN network along with instance-level constraints, such as classification loss and triplet loss [1], [24], [29], guiding the network to learn discriminative identity representations. However, the instance-level similarity measures still suffer from the underlying distribution gap caused by different imaging modalities [20], [32]. Although some recent works propose to employ distribution constraints such as Maximum Mean Discrepancy (MMD) [33] to perform global cross-modality alignment, yet these methods neglect to consider the instance-level distribution variance [14].

In addition, previous cross-modality approaches [18], [23], [24], [26]–[29] usually encode the whole pedestrian image into a feature vector, whereas it is easily contaminated by complex backgrounds and occlusions [30], also, some discriminative local details on human body might be submerged in the learned global descriptors [34], [35]. Most recently, Ye *et al.* [30] introduce a part-based discriminative feature learning method, which evenly divides the feature map into non-overlapping parts and mines contextual relations with attention mechanism. The encouraging performance proves that both part-based features and their relationships are effective for discriminative feature learning in cross-modality task. Nevertheless, this uniform partition strategy is sensitive to pose variations and heavy occlusions [36], [37], which fails to learn features accurately aligned to full body [35].

This paper presents a Geometry-Guided Dual-Alignment ( $G^2DA$ ) learning framework, which could precisely locate body parts and incorporate human-topology relations to augment the discriminability of representations. A sample-level distribution constraint is further introduced to explicitly reduce the modality gap within each class. Concretely, we apply a pose estimation model to extract accurate body parts features. When aligning two categories of features, we cast modality alignment as a graph matching problem. By converting multi-level features into a graph, a novel Graph Optimal Transport (GOT) [38] is introduced to achieve the minimization of distribution divergence between two modalities. As depicted in Fig. 2 (b), the cost matrixs not only measure pairwise distance between two modalities but also compare the structural similarity of part features, effectively facilitating instance-level modality alignment [39]. To handle noisy pose

detections, we advance a geometry-guided graph attention network (GAT) to refine part features with topology relations (i.e., the geometry dependencies of parts, Fig. 2 (c)) [40]. Multi-head attention mechanism [41] is integrated to extract distinct partial-representations from multiple subspaces for diverse salient features [42], [43]. Furthermore, we design a channel-wise message fusion module to dynamically replace the redundant channels, boosting the expressive capacity of learned partial-representations [44]. Extensive experiments on two public datasets validate the superiority of the proposed method, yielding competitive performance compared to the state-of-the-art approaches.

Our major contributions are summarized as follows:

- We attempt to investigate sample-level modality difference, and propose an end-to-end framework ( $G^2DA$ ) of jointly bridging the distribution gap within each class and modeling the dependencies among accurate part features to strengthen both invariance and discriminability in learned representations.
- We pose modality alignment as a graph matching problem, in which a novel distribution constraint (GOT) exploiting both pair-wise relations and group-wise structural similarity is introduced to achieve precise sample-level modality alignment.
- A geometry-guided GAT is advanced to capture diverse discriminative features and suppress noisy pose detection, where a parameter-free message fusion module is further incorporated for enhanced expressibility.
- Extensive experimental results demonstrate the effectiveness of the proposed method over the state-of-the-arts on benchmark datasets.

## II. RELATED WORK

### A. RGB-IR Person ReID

RGB-IR person ReID addresses the problem of matching a target person between two heterogeneous modalities, which has witnessed remarkable progress [1], [2], [14], [18], [20]–[30], [45]–[49] in recent years. Aside from intra-modality variations, RGB-IR ReID encounters the additional modality discrepancy resulting from different wavelength ranges of RGB and IR imaging sensors. Wu *et al.* [18] contributed the first cross-modality ReID dataset SYSU-MM01 and presented a deep zero-padding method to evolve modality-specific information. A partially shared two-stream CNN network was advanced in [48], where shallow layers are independent to learn a common feature space, and deep blocks are shared to mine discriminative cues for matching. There also have emerged a lot of metric learning strategies [23], [24], [26], [27], [29], [33] aiming to extract highly discriminative features that robust to heterogeneous modalities as well. Another avenues [2], [14], [20], [21] attempt to transfer image style via GAN to remit pixel-level modality discrepancy, while it is hard to restore the original colors of IR images and the adversarial training is unstable [50]. Unlike previous approaches, Lu *et al.* [28] leveraged both modality-shared and specific information to strengthen the discriminability of the learned representations.

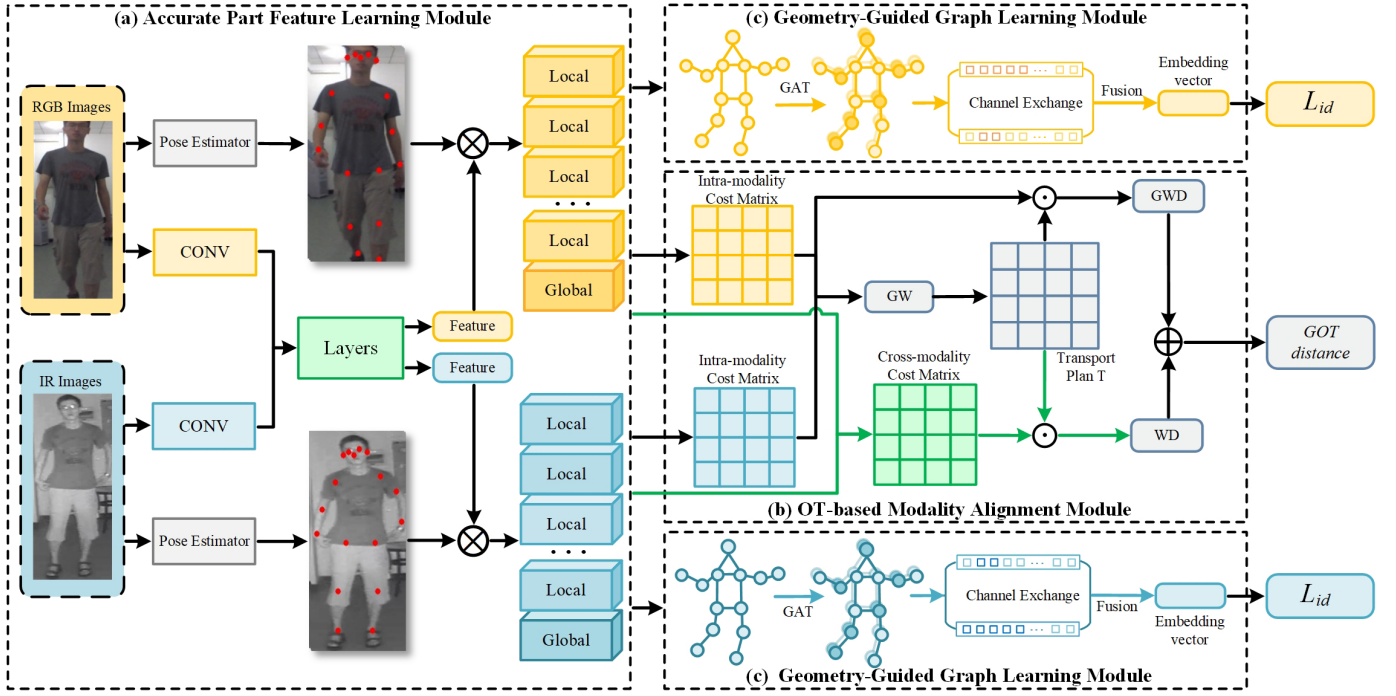


Fig. 2. Illustration of our proposed G<sup>2</sup>DA learning framework. It consists of three modules: (1) **Accurate Part Feature Learning module** extracts multi-level features over human body by incorporating a pose estimator with CNN backbone; (2) **OT-based Modality Alignment module** leverages both pair-wise relations (Cross-modality Cost Matrix) and group-wise structural similarities (Intra-modality Cost Matrix) to evaluate the dissimilarity between heterogeneous distributions; (3) **Geometry-Guided Graph Learning module** employs GAT to emphasize relevant features while suppressing meaningless ones, and a channel-wise message fusion module is further integrated to refine each partial-representation learned by multi-head attention.

However, the modality gap within each class may not be substantially reduced.

### B. Local Feature Representation Learning

To mine as much discriminative cues as possible, most ReID works focus their efforts on local feature learning. Horizontal division [51], [52] usually partition the image into several equal horizontal strips from top to bottom, while the predefined rigid grids are sensitive to pose variations, imperfect pedestrian detectors and heavy occlusions [35]–[37]. Human pose estimation [53]–[55] can alleviate the problem, but might suffer from noisy pose detections. Nevertheless, part-based feature learning is rarely seen in current RGB-IR ReID literature. More recently, Ye *et al.* [30] made the first attempt to learn part-aggregated feature with the uniform partition strategy in RGB-IR ReID task. For better part-level alignment, our study leverages pose landmarks to extract accurate part features over human body, achieving a considerable boost in performance.

### C. Optimal Transport

Optimal Transport (OT) provides a framework to measure the distribution divergence between two domains, aiming to learn a transport plan ( $T$ ) that maps the unit quality from one domain to another with minimal cost [56]. With the success of Wasserstein GAN [57], OT distance, a.k.a Earth Mover’s distance (EMD), has been widely applied to various deep learning tasks [56], [58], [59], [59]–[62]. More recently,

some works [38], [61], [63], [64] attempted to tackle cross-domain alignment problem with OT distance to quantify the relations between cross-domain entities and have produced better results. In this study, we extend OT distance for explicitly handling the modality discrepancy between visible and infrared images.

### D. Graph Attention Network

Inspired by the success of attention mechanism in many sequence-based tasks [65], [66], Velickovic *et al.* [40] extended self-attention strategy to graph learning network and introduce an attention-based architecture, known as Graph Attention Network (GAT). Due to its powerful modeling ability, GAT has been widely used in various fields, e.g., recommendation system [67], [68] and computer vision [69]–[71]. Compared to Graph Convolutional Network (GCN), GAT assigns different weights to nodes connected with the same neighborhood, and the learned attention weights greatly ameliorate the model interpretability. This paper makes the first attempt to leverage GAT to model the dependencies among body part features and extend channel exchanging to multi-head attention to further enhance the discriminative capacity of the learned representations.

## III. PROPOSED METHOD

### A. Problem Formulation

RGB-IR person ReID can be formulated as a cross-modality image retrieval problem, where query and gallery set are in

different modalities. Formally, given a query IR image  $x^I$  of a person  $y_q$ , RGB-IR ReID targets to obtain a ranking list  $\{(x_1^R, y_1), (x_2^R, y_2), \dots, (x_n^R, y_n)\}$  from the RGB gallery set, where  $(x_i^R, y_i)$  indicate a gallery image  $x_i^R$  with its corresponding identity label  $y_i$  ( $i$  is the sorted image index). According to the retrieval formulation, images with label  $y_q$  should appear on the top of the list.

To achieve this goal, the learned representations  $\mathbf{f}$  of the same identity are expected to be closer while that of different classes are further. However, the inherent modality heterogeneity of cross-modality task can result in large intra-class distance. One typical solution is to define a distribution constraint  $\mathcal{D}(\cdot, \cdot)$  and minimize it to push two probability distribution as close as possible [72]. The learning objective can be formulated as:

$$\mathcal{O}_d(\mathbf{f}^R, \mathbf{f}^I) = \min \mathcal{D}(\mathbf{f}^R, \mathbf{f}^I). \quad (1)$$

However, in practical scenarios, RGB-IR ReID still suffers person misalignment arisen from various poses, viewpoints and occlusions, which are further exacerbated by the modality gap in cross-modality setting, making it hard to learn an ideal global descriptor robust to misalignment errors [73]. In this context, local body-parts are less sensitive to background clutter, compared to global descriptors, showing great benefits in handling modality discrepancy. Therefore, we denote the representation of each part as  $\mathbf{f}_k^m$ , where  $m \in \{R, I\}$  is the modality label and  $k \in [1, K]$  ( $K$  is the number of key-points). Here, a part-level constraint  $\mathcal{L}(\cdot, \cdot)$  is designed to enforce feature alignment across two modalities, which can be formulated as:

$$\mathcal{O}_p(\mathbf{f}_k^R, \mathbf{f}_k^I) = \min \mathcal{L}(\mathbf{f}_k^R, \mathbf{f}_k^I). \quad (2)$$

By minimizing the above two loss functions, not only distribution divergence is mitigated but also part-level features alignment between two modalities are guaranteed, i.e.,

$$\mathcal{O}(\mathbf{f}^R, \mathbf{f}^I) = \min(\mathcal{D}(\mathbf{f}^R, \mathbf{f}^I) + \sum_{k=1}^K \mathcal{L}(\mathbf{f}_k^R, \mathbf{f}_k^I)). \quad (3)$$

### B. Accurate Part Feature Learning Module

Prior works mainly dedicate to learning global descriptors that depict the whole images but less robust to noisy images [30], which is even harder to learn in the cross-modal context. Here, we propose to extract accurate body-part features  $\mathbf{f}_k^m$  with the aid of a pose estimation model, where structural information about human pose can be discovered and exploited. Compared to uniform partition strategy [30], the learned human parts can release some difficulties in part-based representations, such as pose variances, background clutters and person misalignment [36], [74].

**Two-stream network.** We adopt a two-stream CNN baseline network to learn a shared feature subspace where heterogeneous images are mapped as modality-invariant features (Fig. 2 (a)). The parameters of the first convolutional block are independent to map multi-modal data into a common subspace, while deep convolutional blocks are shared to mine discriminative features for cross-modality matching. After

global average pooling (GAP), a shared batch normalization (BN) layer is utilized for modality-sharable feature embedding [30]. We combine identity loss  $\mathcal{L}_{id}$  with hard-mining triplet loss  $\mathcal{L}_{tri}$  [75] to optimize the network. The former is a softmax cross-entropy loss used for identity classification, and the latter encourages the distance between positives to get closer while negatives farther. Note that positives (negatives) are sample pairs of different modalities.

$$\mathcal{L}_b = \mathcal{L}_{id} + \mathcal{L}_{tri}. \quad (4)$$

**Pose estimation model.** To obtain accurate localization of human body parts, we employ pre-trained HR-Net [55] as pose estimator to generate thirteen key-points heatmap  $F_{kp} \in \mathbb{R}^{H \times W}$  for every input image. For each  $F_{kp}$ , we copy 2048 copies and then perform outer product ( $\otimes$ ) with  $F_{cnn} \in \mathbb{R}^{2048 \times H \times W}$  extracted from baseline network, respectively, to attain a group of key-points features ( $V_l^m$ ). The global feature ( $V_g^m$ ) is obtained by a global average pooling ( $g_{avg}(\cdot)$ ) and a global max pooling ( $g_{max}(\cdot)$ ) operation. The output features can be formulated as:

$$\begin{aligned} V_l^m &= \{v_k^m\}_{k=1}^K = g_{avg}(F_{cnn} \otimes F_{kp}), \\ V_g^m &= v_{K+1}^m = g_{avg}(F_{cnn}) + g_{max}(F_{cnn}), \end{aligned} \quad (5)$$

here,  $K$  denotes the number of key-point,  $m \in \{R, I\}$  indicates the modality,  $v_k^m \in \mathbb{R}^d$  and  $d$  is the feature dimension.

### C. OT-based Modality Alignment Module

Most of current methods primarily employ instance-level constraints (e.g., contrastive loss [24] and triplet loss [1], [28], [30], [76]) to optimize the relationship of RGB-IR samples, whereas the distribution divergence between modalities still impairs the modality-invariance of features. Therefore, it is reasonable to additionally introduce a distribution constraint to minimize the modality gap [77]. To our understanding, an ideal common subspace should preserve the consistency of global features and local features, as well as their relationships. However, the simple KL and JS divergence are unable to measure the inherent structural relations of the data (e.g., the dependencies of part features). Alternatively, Optimal Transport (OT) served as a distribution measure in which the goal is to learn a transport plan ( $T$ ) that minimizes the cost of transferring the embedding distributions from one domain to another. In this module, we formulate cross-modality alignment as a graph matching problem, and introduce a novel Graph Optimal Transport (GOT) [38] to close the distribution gap between two graphs, thereby realizing the learning objective  $\mathcal{O}_d$ . Rather than global-level alignment, our work achieves fine-grained sample-level alignment by explicitly imposing GOT on image pairs of the same identity.

More specifically, in each modality, we convert the extracted multi-level feature embeddings into a graph, where node is the feature embeddings ( $V_l^m$  and  $V_g^m$ ) and edge indicates the structural similarity between two nodes. To ensure precise graph matching, Wasserstein distance (WD) [78] is used to align node embeddings for its ability to measure point-wise distance, and Gromov-Wasserstein distance (GWD) [79] is employed to guide graph matching in a relational manner

(i.e., edge alignment) by virtue of it could exploit topological information embedded in the graph [38], [64]. With it, not only pair-wise relations across two modalities are measured but also the structural similarity of different parts are modeled, effectively facilitating fine-grained modality alignment in shared space.

**Node alignment.** We utilize WD to match two groups of local features across heterogeneous modalities. Specifically, let  $\mathbb{S}^R$  and  $\mathbb{S}^I$  be complete metric spaces (e.g., Euclidean space),  $\mu \in P(\mathbb{S}^R)$  and  $\nu \in P(\mathbb{S}^I)$  denote two discrete probability distributions,  $\prod(\mu, \nu)$  denote the space of joint probability distributions with marginals  $\mu$  and  $\nu$ . Given two sets of feature vectors  $V^R = V_l^R \cup V_g^R$  and  $V^I = V_l^I \cup V_g^I$  associated with a same identity  $y_i$  from  $\mathbb{S}^R$  and  $\mathbb{S}^I$  respectively, we use WD to promote alignment between two sets of embeddings. The transport plan  $T$  seeks a joint probability distributions  $\gamma \in \prod(\mu, \nu)$  that yields a minimal displacement cost:

$$\begin{aligned} D_w(\mu, \nu) &= \inf_{\gamma \in \prod(\mu, \nu)} \mathbb{E}_{(v^R, v^I) \sim \gamma} [c(v^R, v^I)] \\ &= \min_{T \in \prod(u, v)} \sum_{i=1}^{K+1} \sum_{j=1}^{K+1} T_{ij} \cdot c(v_i^R, v_j^I), \end{aligned} \quad (6)$$

here  $\prod(u, v) = \{T \in \mathbb{R}^{(K+1) \times (K+1)} \mid T \mathbf{1}_{K+1} = u, T^\top \mathbf{1}_{K+1} = v\}$  (vector  $\mathbf{1}_{K+1} = [1, \dots, 1]^\top \in \mathbb{R}^{K+1}$ ),  $v_i^R \in V^R$  and  $v_j^I \in V^I$ . The weight vectors  $u = \{u_i\}_i^{K+1} \in \Delta_{K+1}$  and  $v = \{v_i\}_i^{K+1} \in \Delta_{K+1}$  are  $(K+1)$ -dimensional simplex.  $c(\cdot, \cdot)$  is the cost function (e.g., cosine similarity) that measures the distance between two groups of feature  $V^R$  and  $V^I$ , forming a *Cross-Modality Cost Matrix* as seen in Fig. 2(b).

We further impose a multi-level contrastive loss [80], [81] over every pair of aligned features for Equation (2), which enforces intra-class feature compactness whereas inter-class separability. Different from previous methods, the contrastive loss is applied to both part-based features and global features, where every pair-wise features is of different modalities.

$$L_c = \frac{1}{2N_t(K+1)} \sum_{k=1}^{K+1} \sum_{n=1}^{N_t} (1-y_n) d_{n,k}^2 + y_n \{\max(\varepsilon - d_{n,k}, 0)\}^2, \quad (7)$$

here  $N_t$  is the training batch size, and  $d_{n,k} = \|v_{n,k}^R - v_{n,k}^I\|_2$ .  $y_n$  is a binary label indicating whether two images belong to the same identity,  $y_n = 0$  means they are paired images and  $y_n = 1$  otherwise.  $\varepsilon$  is a predefined margin, which is set to 2.0 in our experiments. Only if  $y_n = 1$  and their distance is smaller than  $\varepsilon$ , the latter term will be incurred.

**Edge alignment.** As for structural similarity, we take both local-local and global-local relations into account, where the former reflects the topology of human body while the latter with a large receptive field offers context guidance for local features. This structure constraint can be used to preserve the relation consistency in the common space. To this end, we employ GWD to quantify these relationships between pairs of nodes, comparing these distance to those in the counterpart modality [38] — in each modality, we calculate the similarity scores between node embeddings (the *Intra-Modality Cost Matrix* shown in the Fig. 2). The scores can be viewed as the edge between two nodes, and edge alignment encourages

both local and global relations across two modalities to be consistent in the common subspace. Following the definition in Eq.(6), we calculate the Gromov-Wasserstein distance as follows:

$$\begin{aligned} D_{gw}(\mu, \nu) &= \inf_{\gamma \in \prod(\mu, \nu)} \mathbb{E}_{(V^R, V^I) \sim \gamma, (V^{R'}, V^{I'}) \sim \gamma} [\mathcal{L}(V^R, V^I, V^{R'}, V^{I'})] \\ &= \min_{T \in \prod(u, v)} \sum_{i,i',j,j'} T_{ij} T_{i'j'} \mathcal{L}(v_i^R, v_j^I, v_{i'}^{R'}, v_{j'}^{I'}), \end{aligned} \quad (8)$$

where  $\mathcal{L}(\cdot)$  is the cost function used to calculate the structural similarity between two pairs of part features  $(v_j^R, v_{j'}^{R'})$  and  $(v_j^I, v_{j'}^{I'})$ , formulated as:  $\mathcal{L}(v_i^R, v_j^I, v_{i'}^{R'}, v_{j'}^{I'}) = \|c(v_i^R, v_{i'}^{R'}) - c(v_j^I, v_{j'}^{I'})\|$ . Note that the learned transport plan  $T$  for GWD is shared with WD. In this way, both node and edge information are exploited to achieve precise graph matching. The unified learning object can be formulated as:

$$D_{ot}(\mu, \nu) = \min_{T \in \prod(u, v)} [\phi D_w(\mu, \nu) + (1 - \phi) D_{gw}(\mu, \nu)], \quad (9)$$

where  $\phi$  is a hyper-parameter to control the importance of two distances. In this way, the modality discrepancy of the same identity can be further alleviated. Meanwhile, the relation of part feature within modality is also maintained.

#### D. Geometry-Guided Graph Learning Module

Considering the intrinsic structure of human body, we design a geometry-guided graph attention network (GAT) [40] to optimize the similarity relations of all the part features [82].

**Graph construction.** Regarding the multi-level features in each modality, we construct an undirected graph  $G = (V, E)$ , where  $V$  represents node set  $V^m = V_l^m \cup V_g^m$  ( $m \in \{R, I\}$ ) and  $E$  is a set of edges that formulates an adjacency matrix  $A \in \{0, 1\}^{(K+1) \times (K+1)}$ .  $A_{i,j} = 1$  means that the  $i$ -th and the  $j$ -th parts are connected and 0 otherwise. Notably, aside from local-local relations, we also model global-local relations by connecting global features with all of local features. In this way, global features provide context guidance (e.g., body shape, gender and clothes) to improve local features [83], and local details, in turn, complement the global features with dispersive fine-grained identity information (e.g., hair, face and feet) [84].

**Node embedding Layer.** With prior knowledge of body structure embedded in graph, each node is allowed to attend over its connected nodes, thus learning a set of parameters (i.e., the attention scores) used to aggregate its corresponding neighbors for node updating. During the training process, the message passing of meaningless nodes (e.g., part features of occluded regions) should be suppressed whilst that of semantic features is promoted. Worthy of mention is that we use multi-head attention mechanism [41], rather than a single attention function, to capture diverse relevant features, in which different body regions (e.g., the head, upper body and lower body) can be parallelly attended by multiple heads.

Given the input node embeddings  $V_k = \{v_k \in \mathbb{R}^d\}_{k=1}^{K+1}$  ( $d$  is the feature dimension), we define a learnable attention coefficient between every pair of nodes to evaluate their similarities. Assume that there are  $L$  attention heads, for the



$l$ -th attention head, the attention coefficients between the  $i$ -th and the  $j$ -th node  $\alpha_{i,j}^l$  can be formulated as:

$$\alpha_{i,j}^l = \frac{\exp(\Gamma(\bar{a}^l[W \cdot v_i \parallel W \cdot v_j]))}{\sum_{\forall A_{i,k}=1} \exp(\Gamma(\bar{a}^l[W \cdot v_i \parallel W \cdot v_k]))}, \quad (10)$$

where  $\Gamma(\cdot)$  denotes the LeakyReLU activation function,  $\bar{a}^l \in \mathbb{R}^{2d}$  is a learnable weight vector of attention mechanism  $a^l$ ,  $W$  is a weight matrix used for feature dimension transformation, and  $\parallel$  indicates the concatenation operation. For the  $i$ -th node, we calculate the attention coefficients with all of its neighbors for aggregation, resulting in a partial-representation of the  $l$ -th head:

$$v_{i,l} = \sigma\left(\sum_{\forall A_{i,j}=1} \alpha_{i,j}^l \cdot W^l \cdot v_j\right), \quad (11)$$

where  $\sigma(\cdot)$  is a nonlinear activation function, and  $W^l$  is the corresponding input linear transformation's weight matrix.

Instead of simply concatenating the learned partial-representations as the final node embedding, we introduce a channel-wise message fusion strategy [44], which enables redundant channels to be adaptively replaced by a meaningful one and thus augment the expressive ability of each partial-representation. Concretely, for the calculated  $v_{i,l}$ , we apply batch normalization (BN) operation with the following affine transformation:

$$v'_{i,l,c} = \gamma_{i,l,c} \frac{v_{i,l,c} - \mu_{i,l,c}}{\sqrt{\sigma_{i,l,c}^2 + \epsilon}} + \beta_{i,l,c}. \quad (12)$$

Here, the subscript  $c$  denotes the  $c$ -th channel;  $\mu_{i,l,c}$  and  $\sigma_{i,l,c}$  are the mean and standard deviation of the  $c$ -th channel for all the  $L$  attention heads;  $\gamma_{i,l,c}$  and  $\beta_{i,l,c}$  are the learnable scaling factor and offset, respectively;  $\epsilon$  is a small constant that used to avoid zero denominator. Note that, the scaling factor  $\gamma_{i,l,c}$  evaluates the importance of the  $c$ -th channel, which implies that  $v'_{i,l,c}$  is potentially redundant if  $\gamma_{i,l,c}$  is very close to a pre-defined threshold [44]. To this end, the adaptive channel exchange can be formulated as:

$$v'_{i,l,c} = \begin{cases} \gamma_{i,l,c} \frac{v_{i,l,c} - \mu_{i,l,c}}{\sqrt{\sigma_{i,l,c}^2 + \epsilon}} + \beta_{i,l,c}, & \text{if } \gamma_{i,l,c} > \theta \\ \frac{1}{L-1} \sum_{l' \neq l} \gamma_{i,l',c} \frac{v_{i,l',c} - \mu_{i,l',c}}{\sqrt{\sigma_{i,l',c}^2 + \epsilon}} + \beta_{i,l',c}, & \text{else} \end{cases} \quad (13)$$

where  $\theta$  is a pre-defined threshold, and a channel should be replaced by the mean of other channels if its scaling factor  $\gamma_{i,l,c}$  is smaller than  $\theta$ . Once all the enhanced partial-representations  $v'_{i,l}$  are obtained, a better output node embedding  $\bar{v}_i$  can be returned via a concatenation operation.

**Aggregation Layer.** To aggregate the learned node features into a unified embedding, an aggregation module is adopted as follows:

$$V_G = BN(g_{avg}(F_{cnn})) + \sum_{k=1}^{K+1} \omega_k \bar{v}_k, \quad (14)$$

here,  $V_G$  is the final graph embedding used to perform retrieval task, and  $BN(\cdot)$  is the batch normalization operation.  $\omega_k$

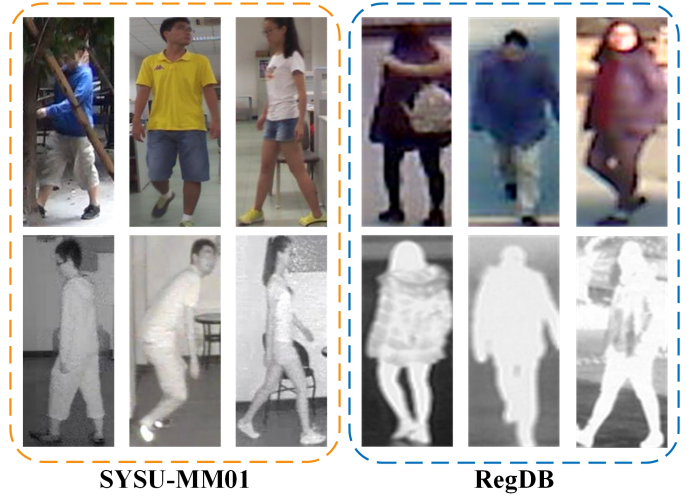


Fig. 3. Example images randomly sampled from SYSU-MM01 [16] and RegDB [19] datasets. The top row is RGB images captured by visible cameras, while the bottom row is the IR images captured by near-infrared cameras on SYSU-MM01 and far-infrared cameras on RegDB, respectively.

is a learnable weight vector meaning that each key-point is assigned to a different weight, where meaningless part features are expected to get small weight.

#### E. Train and Test

The overall framework is trained by the following objective functions:

$$\mathcal{L} = \lambda_b \mathcal{L}_b + \lambda_o D_{ot}(\mu, \nu) + \lambda_c \mathcal{L}_c + \lambda_{id} \mathcal{L}_{id}, \quad (15)$$

where  $\lambda_b$ ,  $\lambda_o$ ,  $\lambda_c$  and  $\lambda_{id}$  are trade-off parameter that indicate the weight of corresponding loss function.

In the testing phase, only *Accurate Part Feature Learning Module* and *Geometry-Guided Graph Learning Module* are adopted, and the final graph embedding  $V_G$  is utilized to perform re-identification. The *OT-based Modality Alignment Module* is employed for optimization alone.

## IV. EXPERIMENT

We evaluate the proposed method on two cross-modality ReID datasets (SYSU-MM01 and RegDB), performing fair comparison with state-of-the-art methods. The ablation study also carried out to validate the effects of each component.

#### A. Experimental Settings

**Datasets.** SYSU-MM01 [16] is a large-scale RGB-IR dataset containing RGB and IR images of 491 identities captured by four visible and two near-infrared cameras under both indoor and outdoor scenes. We adopt the fixed split that using 395 identities with 22,258 RGB images and 11,909 IR images for training and 96 identities for testing. Following the evaluation protocol [16], there are two search modes, i.e., *all-search* and *indoor-search*. The former contains images

TABLE I

COMPARISON WITH THE STATE-OF-THE-ARTS ON SYSU-MM01 DATASET UNDER TWO SEARCH MODES. ACCURACY (%) AT RANK R AND MAP ARE REPORTED.

Method	All-search								Indoor-search							
	Single-shot				Multi-shot				Single-shot				Multi-shot			
	r1	r10	r20	mAP	r1	r10	r20	mAP	r1	r10	r20	mAP	r1	r10	r20	mAP
HOG [85]	2.76	18.3	31.9	4.24	3.82	22.8	37.6	2.16	3.22	24.7	44.5	7.25	4.75	29.2	49.4	3.51
LOMO [86]	3.64	23.2	37.3	4.53	4.70	28.2	43.1	2.28	5.75	34.4	54.9	10.2	7.36	40.4	60.3	5.64
Zero-Padding [18]	14.8	54.1	71.3	15.9	19.1	61.4	78.4	10.9	20.6	68.4	85.8	26.9	24.4	75.9	91.3	18.6
TONE+HCML [24]	14.3	53.2	69.2	16.2	-	-	-	-	-	-	-	-	-	-	-	-
BDTR [23]	17.0	55.4	72.0	19.7	-	-	-	-	-	-	-	-	-	-	-	-
D-HSME [26]	20.7	62.8	78.0	23.2	-	-	-	-	-	-	-	-	-	-	-	-
IPVT+MSR [45]	23.2	51.2	61.7	22.5	-	-	-	-	-	-	-	-	-	-	-	-
cmGAN [25]	27.0	67.5	80.6	27.8	31.5	72.7	85.0	22.3	31.6	77.2	89.2	42.2	37.0	80.9	92.1	32.8
D <sup>2</sup> RL [20]	28.9	70.6	82.4	29.2	-	-	-	-	-	-	-	-	-	-	-	-
DGD+MSR [47]	37.4	83.4	93.3	38.1	43.9	86.9	95.7	30.5	39.6	89.3	97.7	50.9	46.6	93.6	98.8	40.1
JSIA-ReID [14]	38.1	80.7	89.9	36.9	45.1	85.7	93.8	29.5	43.8	86.2	94.2	52.9	52.7	91.1	96.4	42.7
AlignGAN [2]	42.4	85.0	93.7	40.7	51.5	89.4	95.7	33.9	45.9	87.6	94.4	54.3	57.1	92.7	97.4	45.3
AGW [37]	47.5	84.39	92.14	47.65	-	-	-	-	54.17	91.14	95.98	62.97	-	-	-	-
Xmodal [76]	49.92	89.79	95.96	50.73	-	-	-	-	-	-	-	-	-	-	-	-
DDAG [30]	54.75	90.39	95.81	53.02	61.83	92.68	97.49	47.06	61.02	94.06	<b>98.41</b>	67.98	69.23	95.13	98.31	59.42
Ours	<b>57.07</b>	<b>90.99</b>	<b>96.28</b>	<b>55.05</b>	<b>64.47</b>	<b>94.22</b>	<b>98.18</b>	<b>48.91</b>	<b>63.70</b>	<b>94.06</b>	98.35	<b>69.83</b>	<b>72.62</b>	<b>95.99</b>	<b>98.87</b>	<b>61.89</b>

captured by all four visible cameras and the latter only comprises images captured by two indoor visible cameras. For each mode, we adopt both *single-shot* and *multi-shot* settings, which means that the gallery set contains one/ten randomly selected RGB image(s) for each IR query image. It is worth noting that *single-shot* & *all-search* is the most challenging test mode.

RegDB [19] is a relatively small-scale dataset collected by a dual-camera system (one visible and one far-infrared). We present some samples from two datasets to illustrate the difference of IR images captured by near-infrared and far-infrared cameras (Fig. 3). RegDB accommodates 8240 images of 412 identities, where each identity has 10 RGB and 10 IR images, respectively. We randomly divide the dataset into two halves, one for training and the other for testing, and repeated a total of 10 times random splits of the gallery and probe sets [24]. During the test stage, both *Visible-to-Thermal* and *Thermal-to-Visible* evaluation modes are adopted.

**Evaluation Protocols.** To evaluate the performance of our model, Cumulative Matching Characteristic (CMC) curve and mean Average Precision (mAP) are adopted as the evaluation criteria. The CMC at rank-k represents the probability of the correct match occurs in top-k retrieval results, and mAP is a comprehensive evaluation measuring the retrieval performance of multi-matching. Different from the conventional ReID task, during the testing stage, the query set and gallery set are of different modalities in cross-modality tasks.

**Implementation details.** The proposed method is developed on Pytorch framework with NVIDIA 2080Ti GPU. Following existing RGB-IR ReID works [30], [37], we adopt a two-stream CNN network with ResNet50 backbone for fair comparison [87], and apply the parameters pre-trained on

ImageNet [88] for network initialization. Specifically, the parameters are different in the first block, while deep convolutional blocks are shared for each modality. As for the pose estimation model, we adopt the state-of-the-art HR-Net [55] pre-trained on the COCO dataset [89] and get  $K = 14$  key-points including head, shoulders, elbows, wrists, hips, knees, and ankles, following [90]. Multi-head attention mechanism is adopted to optimize the similarity relationships of part features, where the number of attention heads  $L$  is set to 4.

Both in training and testing stage, the input images are firstly resized to  $288 \times 144$ , and random cropping with zero-padding and horizontal flipping are adopted for data augmentation [30]. The batch size  $N_t$  is set to 64, and each identity comprises 4 RGB and 4 IR images, for a total of 8 identities. We set the learning rate as 0.1 for both datasets, which is decayed by 0.1 at 30-th epoch and 0.01 at 50-th epoch. Our model is trained with total 80 epochs and is optimized with stochastic gradient descent (SGD), where momentum parameter is set to 0.9. By default, we set the margin parameter  $\rho$  in triplet loss to 0.3,  $\varepsilon$  in contrastive loss to 2.0 and  $\theta$  in channel exchange to 0.02, the hyper-parameter  $\phi$  in Equation (9) to 0.5. The trade-off parameter  $\lambda_b = 1$ ,  $\lambda_o = 1$ ,  $\lambda_c = 0.1$  and  $\lambda_{id} = 1$ .

### B. Comparison With the State-of-the-Arts

In this subsection, we conduct a thorough comparison of the proposed method with both conventional and state-of-the-art methods, including HOG [85], LOMO [86], Zero-Padding [18], TONE+HCML [24], BDTR [23], D-HSME [26], IPVT+MSR [45], cmGAN [25], D<sup>2</sup>RL [20], DGD+MSR [47],

TABLE II  
COMPARISON WITH THE STATE-OF-THE-ARTS ON REGDB DATASET WITH TWO TEST MODES. ACCURACY (%) AT RANK R AND mAP ARE REPORTED.

Method	Visible to Thermal				Thermal to Visible			
	r1	r10	r20	mAP	r1	r10	r20	mAP
Zero-Padding [18]	17.75	34.21	44.35	18.90	16.63	34.68	44.25	17.82
TONE + HCML [24]	24.44	47.53	56.78	20.88	21.70	45.02	55.58	22.24
BDTR [23]	33.56	58.61	67.43	32.76	32.92	58.46	68.43	31.96
D <sup>2</sup> RL [20]	43.40	66.10	76.30	44.10	-	-	-	-
DGD+MSR [47]	48.43	70.32	79.95	48.67	-	-	-	-
JSIA-ReID [14]	48.10	-	-	48.90	48.50	-	-	49.30
D-HSME [26]	50.85	73.36	81.66	47.00	50.15	72.40	81.07	46.16
IPVT+MSR [45]	58.76	85.75	90.27	47.85	-	-	-	-
AlignGAN [2]	57.90	-	-	53.60	56.30	-	-	53.40
Xmodal [76]	62.21	83.13	91.72	60.18	-	-	-	-
AGW [37]	70.05	-	-	<b>66.37</b>	-	-	-	-
DDAG [30]	69.34	86.19	91.49	63.46	68.06	<b>85.15</b>	<b>90.31</b>	61.80
Ours	<b>71.72</b>	<b>87.13</b>	<b>91.92</b>	65.90	<b>69.50</b>	84.87	89.85	<b>63.88</b>

TABLE III  
ABLATION STUDY ON SYSU-MM01 DATASET UNDER TWO SEARCH MODES. ACCURACY (%) AT RANK R AND mAP ARE REPORTED.

Search modes	All-search				Indoor-search			
Methods	r1	r10	r20	mAP	r1	r10	r20	mAP
<i>B</i>	49.17	84.38	92.16	47.27	53.60	89.67	95.63	61.41
<i>B+O</i>	53.58	88.26	94.27	52.00	57.13	92.23	97.55	64.86
<i>B+O+CL</i>	54.56	88.89	95.05	53.52	57.74	93.47	98.09	65.69
<i>B+O+CL+G</i>	56.65	90.84	96.18	54.83	61.80	93.85	97.93	68.77
<i>B+O+CL+G+CE</i>	57.07	90.99	96.28	55.05	63.70	94.06	98.35	69.83

JSIA-ReID [14], AlignGAN [2], AGW [37], Xmodal [76] and DDAG [30].

**Results on SYSU-MM01 dataset.** We adopt both *all-search* and *indoor-search* test modes, and each mode is performed in both *single-shot* and *multi-shot* ways. As shown in Table I, our method outperforms state-of-the-art approaches on the most challenging *single-shot* & *all-search* test mode, obtaining 57.50% Rank-1 accuracy and 55.91% mAP scores. Through in-depth analysis, we make the observations as follows: (1) Hand-craft features (HOG, LOMO) cannot well be generalized to the cross-modality matching task; (2) Feature learning with instance-level constraints, such as classification loss, triplet loss and ranking loss, shows significant improvement in performance. Whereas, these learning objectives mainly concentrate on optimizing the relationship between RGB-IR samples, the distribution divergence between two modalities has not been properly solved, which can degenerate the re-identification performance; (3) Adversarial learning-based methods (cmGAN, D<sup>2</sup>RL, JSIA-ReID, AlignGAN) also achieve high re-identification accuracy. Most of them leverage GAN to generate cross-modality images for the reduction of pixel-level modality discrepancy, but they complicate the inference pipeline by appending a pre-processing module, and the adversarial training is unstable [30]. (4) Recent shared feature learning methods (AGW, DDAG) significantly outperform the

state-of-the-art GAN-based method (AlignGAN), which also show considerable efficiency as they are free of adversarial training. Compared to these methods, our work not only introduces a novel distribution constraint to bridge the modality gap within each class, but also exerts the potential effect of human body characteristics, including the accurate body-parts and human topology information, to facilitate discriminative feature learning. The superiority has been validated by the reported experimental results.

**Results on RegDB dataset.** Table II presents the comparison results on RegDB dataset, where both *Visible-to-Thermal* and *Thermal-to-Visible* test modes are adopted. It is clear that our method achieves comparable performance to existing approaches, attaining 71.57% and 69.11% in terms of Rank-1 identification rate under two test modes, respectively, which further verifies that our model is robust to heterogeneous query settings. From the perspective of test mode, the performance of *Visible-to-Thermal* is better than that of *Thermal-to-Visible*, possibly benefiting from rich visual cues containing in visible images.

### C. In-Depth Model Analysis

**Ablation Study.** To verify the contribution of each component to the model, we conduct ablation experiments on standard benchmark SYSU-MM01 dataset with both *all-search*



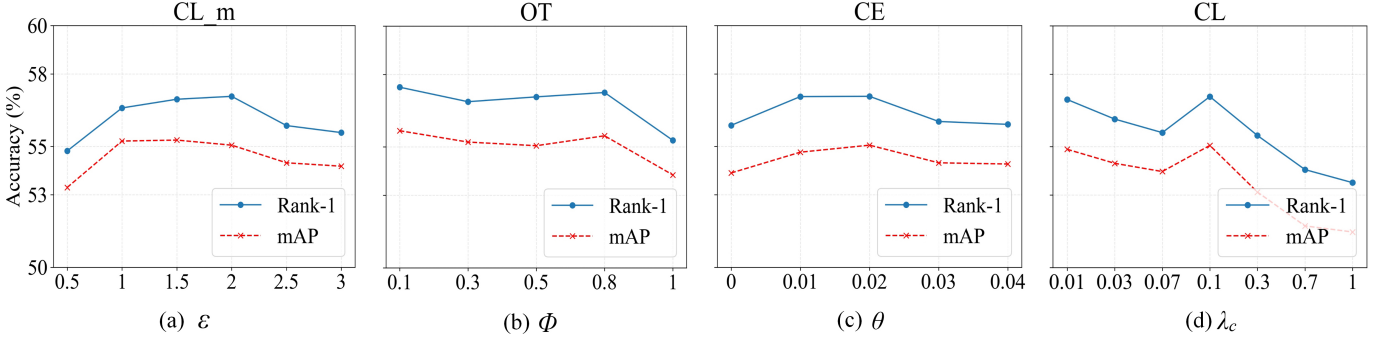


Fig. 4. Evaluation of the margin  $\varepsilon$  of contrastive loss in Equation (7), the hyper-parameter  $\phi$  in Equation (9), the threshold  $\theta$  of channel exchange in Equation (13) and the trade-off parameter  $\lambda_c$  in Equation (15) on SYSU-MM01 dataset with *single-shot* & *all-search* test mode. Rank-1 accuracy (%) and mAP score(%) are reported. Best viewed in color.

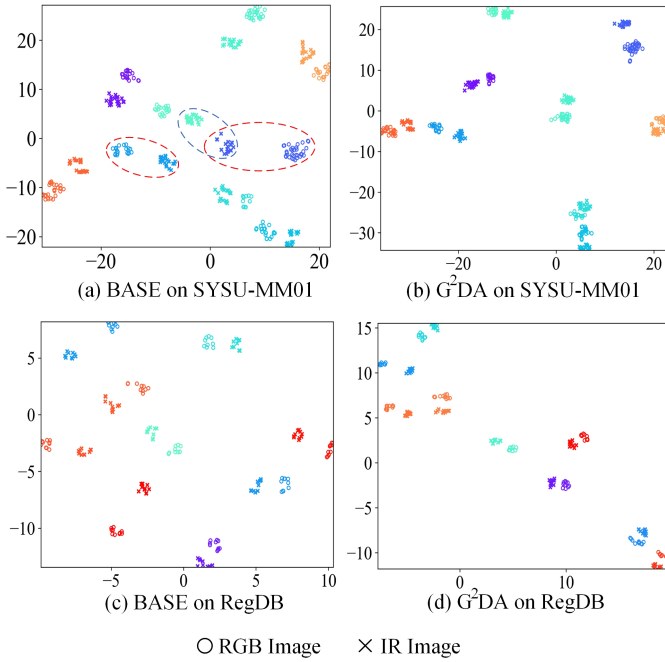


Fig. 5. *t*-SNE visualization of the last hidden layer representations in the CNN learned by baseline model (a)(c) and our method (b)(d) on SYSU-MM01 and RegDB, respectively. The circle and cross shape represent the modality, and each color stands for an identity.

and *indoor-search* modes, and both modes are performed in *single-shot* manner. To be specific, “*B*” denotes the baseline model, a partially shared two-stream CNN network trained by  $L_b$ . “*O*” indicates OT distance. “*CL*” is the contrastive loss. “*G*” indicates the geometry-guided GAT and “*CE*” represents channel exchange. We should note that “*O*”, “*CL*”, “*G*” and “*CE*” are all based on multi-level features extracted by the *Accurate Part Feature Learning Module*. The results are reported in Table III.

We adopt a two-stream CNN network following [30] as our baseline model, where the first residual block is independent for each modality to capture modality-specific feature patterns and the other four blocks are shared to learn modality-shared feature embeddings. The combination of identity loss and

triplet loss guides the network to learn cross-modality discriminative feature representations. It achieves 49.17% and 47.27% in terms of Rank-1 accuracy and mAP score, respectively, outperforming a lot of previous methods and proving to be a strong baseline model.

**Effectiveness of *O*.** Based on *B*, we further employ OT distance to explicitly mitigate the distribution difference of each identity across two modalities, which exhibits a clear improvement over the baseline model by 4.41% on Rank-1 accuracy and 4.73% on mAP score under the challenging *all-search* mode, and a larger improvement can be seen in *indoor-search* mode. It is obvious that the bridge of intra-class distribution gap greatly benefits modality-invariant feature learning, effectively facilitating cross-modality matching.

**Effectiveness of *CL*.** Based on *B+O*, we study the effectiveness of the proposed multi-level contrastive loss, and observe that the performance get a further improved by 0.98% on Rank-1 identification rate and 1.52% on mAP score. The above phenomenon shows the importance of part-level feature alignment, and simultaneously verifies that the proposed contrastive loss enhances the modality-invariance of the learned representations.

**Effectiveness of *G*.** When we further integrate with the proposed geometry-guided GAT, the matching performance is advanced with gains of 2.09% and 4.06% in Rank-1 accuracy under *all-search* and *indoor-search* modes, respectively. Thus, it is evident that the geometry dependencies of body-parts are capable of refining part features, where semantic features are emphasized but meaningless ones are suppressed.

**Effectiveness of *CE*.** We augment the multi-head attention mechanism with a channel-wise message fusion module to reinforce each partial-representation. As we can see, it acquires 1.9% performance gain of on Rank-1 identification rate and 1.06% improvement on mAP score under *indoor-search* mode, demonstrating that it is beneficial to learn high-quality representations.

It is obvious that the proposed model reaches the optimal performance when integrating with all components, obtaining 57.07% on Rank-1 accuracy and 55.05% on mAP score, which suggests that all these modules work well together.

**Parameters Analysis.** This subsection evaluates the effect



Fig. 6. Top-10 retrieval results of randomly selected 10 identities on SYSU-MM01 dataset under two query modes. Green and Red boxes denote correct and wrong matching results, respectively. The number on top of each image represents the similarity to the query image.

of four key parameters in the proposed method, i.e., the margin  $\varepsilon$  of contrastive loss in Equation (7), the hyper-parameter  $\phi$  in Equation (9), the threshold  $\theta$  of channel exchange in Equation (13) and the trade-off parameter  $\lambda_o$  in Equation (15). We implement all the experiments on SYSU-MM01 dataset with the most challenging *single-shot & all-search* test mode. The results are presented in Fig. 4.

(1) The margin  $\varepsilon$  is utilized to define the distance difference between negative sample pairs. We vary  $\varepsilon$  from 0.5 to 3 and evaluate the performance under these settings. It can be observed that either a smaller or a larger  $\varepsilon$  would impair the performance, and  $\varepsilon \in [1.5, 2]$  can achieve better performance.

(2) The hyper-parameter  $\phi$  is used to control the trade-off between WD and GWD. We observe that the re-identification performance could be consistently improved when  $\phi \in [0.1, 0.8]$ , but drops dramatically when only WD works (i.e.,  $\phi = 1$ ). Results in Fig. 4 (b) demonstrate that both WD and GWD are crucial for modality alignment.

(3) The threshold  $\theta$  is designed to determine whether a channel should be exchanged. We investigate the trend of performance when  $\theta$  ranges from 0 to 0.04 ( $\theta = 0$  means that the channel exchange module is removed). It can be seen that both Rank-1 accuracy and mAP score are consistently improved with increasing  $\theta$ , and then decrease after  $\theta = 0.02$ .

(4) The trade-off parameter  $\lambda_c$  indicates the influence of contrastive loss to the retrieval performance, and a proper selection of  $\lambda_c$  is of critical importance. As depicted in Fig. 4 (d), we vary  $\lambda_c$  from 0.01 to 1, and observe that this term could improve the cross-modality ReID accuracy when  $\lambda_c = 0.1$ . This benefit is brought by the further enhancement of intra-class compactness and inter-class separability.

Empirically, we set  $\varepsilon = 2$ ,  $\phi = 0.5$ ,  $\theta = 0.02$  and  $\lambda_c = 0.1$  in all our experiments. Notably, better performance might be achieved by different parameter selection.

#### D. Visualization of results

**Learned Feature Subspace.** To dive deeper into the learned common subspace, we adopt *t*-SNE [91] to visualize the learned feature embeddings of 9 randomly sampled identities on SYSU-MM01 and RegDB datasets, compared with baseline model. We make the observations as follows.

As shown in Fig. 5 (a) and (c), the common feature subspace learned by the baseline model still suffers large intra-class variations and small inter-class distance. This observation demonstrates that it is inadequate to eliminate the large modality gap with instance-level constraints alone, and feature distribution divergence resulted from different sensing mechanisms can impair the discriminability of the learned shared space. As we can see the red dashed circles in Fig. 5 (a), the distance within the class is far from reduced, leading to a phenomenon that intra-class distance is larger than that of inter-class (the blue dashed circle in Fig. 5 (a)).

To handle the above issues, we additionally impose OT distance on aligned features to measure the difference between RGB and IR data distribution, explicitly eliminating the distribution difference of the same identity. The multi-level contrastive loss also effectively improves the relationship between RGB-IR sample pairs. Moreover, the introduced geometry-guided graph learning module further reinforces the learned representation with human topology information. As illustrated in Fig. 5 (b) and (d), the dots of every cluster is tied closely and the clusters of different categories are pushed farther to each other. This visualization obviously demonstrates that the proposed method significantly boost the discriminative ability of the learned feature space.

In the nutshell, our method achieves both intra-class compactness and inter-class separability, proving to be a promising approach for cross-modality retrieval task.

**Retrieval Results.** Following the evaluation protocol of

SYSU-MM01 [16], we only use IR query to retrieve RGB images in Section. IV, i.e., *Thermal-to-Visible* query mode, and achieve the state-of-the-art result. To further validate the effectiveness of the proposed model, we additionally implement our model under *Visible-to-Thermal* query mode and visualize the retrieval results of both query settings. For each query mode, 5 identities are randomly selected and their Top-10 retrieval results are reported.

As shown in Fig. 6, we observe that even most of query images are the person in the back, our model still performs well on both query settings. Compared to *Thermal-to-Visible* mode, the result of *Visible-to-Thermal* mode is much better because visible images contain more visual cues that are conducive to matching. Regarding the challenging *Thermal-to-Visible* mode, although there are matching errors appearing in the ranking list, the correct retrieval results are still ranked to the top. As in the last line of Fig. 6 (b), we surprisingly observe that the accessory cue (i.e., the backpack) is different between query and Rank-1 images. This phenomenon probably benefits from the accurate localization of body-part, which shows robustness to local-appearance variations. To sum up, the visualization results of both query modes further prove that our proposed method effectively augments the modality-invariance and discriminability in learned representations, thereby yielding impressive retrieval accuracy.

## V. CONCLUSION

In this paper, we present a Geometry-Guided Dual-Alignment ( $G^2DA$ ) learning framework to precisely align local body-part features and explicitly bridge the distribution gap within each class. Based on well-aligned part features guided by human pose landmarks, we formulate modality alignment as a graph matching problem by using a novel graph optimal transport distance. In this way, not only pairwise distance between two modalities are measured but also group-wise structural similarities are compared, exhibiting a clear advantage in sample-level modality alignment. Furthermore, we devise a geometry-guided graph attention network to reinforce the part features with human-topology relations, where semantic features are highlighted while meaningless regions are suppressed. A channel-wise message fusion module is further incorporated to augment the expressibility of the learned representations. Extensive experimental results on two standard benchmark datasets validate the effectiveness of our proposed method.

## REFERENCES

- [1] M. Ye, J. Shen, and L. Shao, "Visible-infrared person re-identification via homogeneous augmented tri-modal learning," *IEEE Transactions on Information Forensics and Security*, vol. 16, pp. 728–739, 2021.
- [2] G. Wang, T. Zhang, J. Cheng, S. Liu, Y. Yang, and Z. Hou, "Rgb-infrared cross-modality person re-identification via joint pixel and feature alignment," in *Proceedings of the IEEE/CVF International Conference on Computer Vision (ICCV)*, October 2019.
- [3] F. M. Khan and F. Br  mond, "Person re-identification for real-world surveillance systems," *ArXiv*, vol. abs/1607.05975, 2016.
- [4] R. Vezzani, D. Baltieri, and R. Cucchiara, "People reidentification in surveillance and forensics: A survey," *ACM Computing Surveys*, 12 2013.
- [5] Y. Shen, H. Li, S. Yi, D. Chen, and X. Wang, "Person re-identification with deep similarity-guided graph neural network," in *Proceedings of the European Conference on Computer Vision (ECCV)*, September 2018.
- [6] J. Xu, R. Zhao, F. Zhu, H. Wang, and W. Ouyang, "Attention-aware compositional network for person re-identification," in *Proceedings of the IEEE Conference on Computer Vision and Pattern Recognition (CVPR)*, June 2018.
- [7] C.-P. Tay, S. Roy, and K.-H. Yap, "Aanet: Attribute attention network for person re-identifications," in *Proceedings of the IEEE/CVF Conference on Computer Vision and Pattern Recognition (CVPR)*, June 2019.
- [8] H. Luo, Y. Gu, X. Liao, S. Lai, and W. Jiang, "Bag of tricks and a strong baseline for deep person re-identification," in *Proceedings of the IEEE/CVF Conference on Computer Vision and Pattern Recognition (CVPR) Workshops*, June 2019.
- [9] X. Jin, C. Lan, W. Zeng, Z. Chen, and L. Zhang, "Style normalization and restitution for generalizable person re-identification," in *Proceedings of the IEEE/CVF Conference on Computer Vision and Pattern Recognition (CVPR)*, June 2020.
- [10] M. Ye, X. Lan, and Q. Leng, "Cross-modality person re-identification via modality-aware collaborative ensemble learning," *IEEE Transactions on Image Processing*, vol. 29, pp. 9387–9399, 2020.
- [11] X. Liu, L. Song, X. Wu, and T. Tan, "Transferring deep representation for nir-vis heterogeneous face recognition," *2016 International Conference on Biometrics (ICB)*, pp. 1–8, 2016.
- [12] X. Wu, L. Song, R. He, and T. Tan, "Coupled deep learning for heterogeneous face recognition," in *AAAI*, 2018.
- [13] J. Ma, Y. Ma, and C. Li, "Infrared and visible image fusion methods and applications: A survey," *Inf. Fusion*, vol. 45, pp. 153–178, 2019.
- [14] G. Wang, T. Zhang, Y. Yang, J. Cheng, J. Chang, X. Liang, and Z. Hou, "Cross-modality paired-images generation for rgb-infrared person re-identification," in *AAAI*, 2020.
- [15] F. Huang, L. Zhang, Y. Yang, and X. Zhou, "Probability weighted compact feature for domain adaptive retrieval," *2020 IEEE/CVF Conference on Computer Vision and Pattern Recognition (CVPR)*, pp. 9579–9588, 2020.
- [16] A. Wu, W. Zheng, S. Gong, and J. Lai, "Rgb-ir person re-identification by cross-modality similarity preservation," *International Journal of Computer Vision*, vol. 128, pp. 1765–1785, 2020.
- [17] C. Ding, K. Wang, P. Wang, and D. Tao, "Multi-task learning with coarse priors for robust part-aware person re-identification," *IEEE transactions on pattern analysis and machine intelligence*, vol. PP, 2020.
- [18] A. Wu, W.-S. Zheng, H.-X. Yu, S. Gong, and J. Lai, "Rgb-infrared cross-modality person re-identification," in *Proceedings of the IEEE International Conference on Computer Vision (ICCV)*, Oct 2017.
- [19] T. D. Nguyen, H. Hong, K. Kim, and K. Park, "Person recognition system based on a combination of body images from visible light and thermal cameras," *Sensors (Basel, Switzerland)*, vol. 17, 2017.
- [20] Z. Wang, Z. Wang, Y. Zheng, Y.-Y. Chuang, and S. Satoh, "Learning to reduce dual-level discrepancy for infrared-visible person re-identification," in *Proceedings of the IEEE/CVF Conference on Computer Vision and Pattern Recognition (CVPR)*, June 2019.
- [21] S. Choi, S. Lee, Y. Kim, T. Kim, and C. Kim, "Hi-cmd: Hierarchical cross-modality disentanglement for visible-infrared person re-identification," in *Proceedings of the IEEE/CVF Conference on Computer Vision and Pattern Recognition (CVPR)*, June 2020.
- [22] K. Kansal, A. V. Subramanyam, Z. Wang, and S. Satoh, "Sdl: Spectrum-disentangled representation learning for visible-infrared person re-identification," *IEEE Transactions on Circuits and Systems for Video Technology*, vol. 30, pp. 3422–3432, 2020.
- [23] M. Ye, Z. Wang, X. Lan, and P. Yuen, "Visible thermal person re-identification via dual-constrained top-ranking," in *IJCAI*, 2018.
- [24] M. Ye, X. Lan, J. Li, and P. Yuen, "Hierarchical discriminative learning for visible thermal person re-identification," in *AAAI*, 2018.
- [25] P. Dai, R. Ji, H. Wang, Q. Wu, and Y. Huang, "Cross-modality person re-identification with generative adversarial training," in *IJCAI*, 2018.
- [26] Y. Hao, N. Wang, J. Li, and X. Gao, "Hsme: Hypersphere manifold embedding for visible thermal person re-identification," in *AAAI*, 2019.

- [27] S. Zhang, Y. Yang, P. Wang, X. Zhang, and Y. Zhang, "Attend to the difference: Cross-modality person re-identification via contrastive correlation," *ArXiv*, vol. abs/1910.11656, 2019.
- [28] Y. Lu, Y. Wu, B. Liu, T. Zhang, B. Li, Q. Chu, and N. Yu, "Cross-modality person re-identification with shared-specific feature transfer," in *Proceedings of the IEEE/CVF Conference on Computer Vision and Pattern Recognition (CVPR)*, June 2020.
- [29] M. Ye, X. Lan, Z. Wang, and P. Yuen, "Bi-directional center-constrained top-ranking for visible thermal person re-identification," *IEEE Transactions on Information Forensics and Security*, vol. 15, pp. 407–419, 2020.
- [30] M. Ye, J. Shen, D. J. Crandall, L. Shao, and J. Luo, "Dynamic dual-attentive aggregation learning for visible-infrared person re-identification," *ArXiv*, vol. abs/2007.09314, 2020.
- [31] K. Wang, R. He, L. Wang, W. Wang, and T. Tan, "Joint feature selection and subspace learning for cross-modal retrieval," *IEEE Transactions on Pattern Analysis and Machine Intelligence*, vol. 38, pp. 2010–2023, 2016.
- [32] R. He, X. Wu, Z. Sun, and T. Tan, "Wasserstein cnn: Learning invariant features for nir-vis face recognition," *IEEE Transactions on Pattern Analysis and Machine Intelligence*, vol. 41, pp. 1761–1773, 2019.
- [33] M. Ye, Y. Cheng, X. Lan, and H. Zhu, "Improving night-time pedestrian retrieval with distribution alignment and contextual distance," *IEEE Transactions on Industrial Informatics*, vol. 16, pp. 615–624, 2020.
- [34] Z. Kuang, Y. Gao, G. Li, P. Luo, Y. Chen, L. Lin, and W. Zhang, "Fashion retrieval via graph reasoning networks on a similarity pyramid," in *Proceedings of the IEEE/CVF International Conference on Computer Vision (ICCV)*, October 2019.
- [35] X. Bai, M. Yang, T. Huang, Z. Dou, R. Yu, and Y. Xu, "Deep-person: Learning discriminative deep features for person re-identification," *Pattern Recognition*, vol. 98, p. 107036, 2020. [Online]. Available: <http://www.sciencedirect.com/science/article/pii/S0031320319303395>
- [36] D. Li, X. Chen, Z. Zhang, and K. Huang, "Learning deep context-aware features over body and latent parts for person re-identification," *2017 IEEE Conference on Computer Vision and Pattern Recognition (CVPR)*, pp. 7398–7407, 2017.
- [37] M. Ye, J. Shen, G. Lin, T. Xiang, L. Shao, and S. Hoi, "Deep learning for person re-identification: A survey and outlook," *IEEE transactions on pattern analysis and machine intelligence*, vol. PP, 2021.
- [38] L. Chen, Z. Gan, Y. Cheng, L. Li, L. Carin, and J. jing Liu, "Graph optimal transport for cross-domain alignment," *ArXiv*, vol. abs/2006.14744, 2020.
- [39] H. Xu, D. Luo, H. Zha, and L. Carin, "Gromov-wasserstein learning for graph matching and node embedding," in *ICML*, 2019.
- [40] P. Velickovic, G. Cucurull, A. Casanova, A. Romero, P. Liò, and Y. Bengio, "Graph attention networks," *ArXiv*, vol. abs/1710.10903, 2018.
- [41] A. Vaswani, N. Shazeer, N. Parmar, J. Uszkoreit, L. Jones, A. N. Gomez, L. Kaiser, and I. Polosukhin, "Attention is all you need," in *NIPS*, 2017.
- [42] J. Li, B. Yang, Z.-Y. Dou, X. Wang, M. R. Lyu, and Z. Tu, "Information aggregation for multi-head attention with routing-by-agreement," in *NAACL-HLT*, 2019.
- [43] P.-Y. Huang, X. Chang, and A. Hauptmann, "Multi-head attention with diversity for learning grounded multilingual multimodal representations," *ArXiv*, vol. abs/1910.00058, 2019.
- [44] Y. Wang, W. Huang, F.-C. Sun, T. Xu, Y. Rong, and J. Huang, "Deep multimodal fusion by channel exchanging," *ArXiv*, vol. abs/2011.05005, 2020.
- [45] J. K. Kang, T. M. Hoang, and K. R. Park, "Person re-identification between visible and thermal camera images based on deep residual cnn using single input," *IEEE Access*, vol. 7, pp. 57 972–57 984, 2019.
- [46] N. Tekeli and A. Burak Can, "Distance based training for cross-modality person re-identification," in *Proceedings of the IEEE/CVF International Conference on Computer Vision (ICCV) Workshops*, Oct 2019.
- [47] Z. Feng, J. Lai, and X. Xie, "Learning modality-specific representations for visible-infrared person re-identification," *IEEE Transactions on Image Processing*, vol. 29, pp. 579–590, 2019.
- [48] M. Ye, X. Lan, and Q. Leng, "Modality-aware collaborative learning for visible thermal person re-identification," *Proceedings of the 27th ACM International Conference on Multimedia*, 2019.
- [49] Y. Zhu, Z. Yang, L. Wang, S. Zhao, X. Hu, and D. Tao, "Hetero-center loss for cross-modality person re-identification," *ArXiv*, vol. abs/1910.09830, 2020.
- [50] H. Liu, X. Tan, and X. Zhou, "Parameter sharing exploration and hetero-center triplet loss for visible-thermal person re-identification," *IEEE Transactions on Multimedia*, pp. 1–1, 2020.
- [51] R. Varior, B. Shuai, J. Lu, D. Xu, and G. Wang, "A siamese long short-term memory architecture for human re-identification," *ArXiv*, vol. abs/1607.08381, 2016.
- [52] Y. Sun, L. Zheng, Y. Yang, Q. Tian, and S. Wang, "Beyond part models: Person retrieval with refined part pooling (and a strong convolutional baseline)," in *Proceedings of the European Conference on Computer Vision (ECCV)*, September 2018.
- [53] E. Insafutdinov, L. Pishchulin, B. Andres, M. Andriluka, and B. Schiele, "Deepcrut: A deeper, stronger, and faster multi-person pose estimation model," in *ECCV*, 2016.
- [54] Z. Cao, T. Simon, S.-E. Wei, and Y. Sheikh, "Realtime multi-person 2d pose estimation using part affinity fields," in *Proceedings of the IEEE Conference on Computer Vision and Pattern Recognition (CVPR)*, July 2017.
- [55] K. Sun, B. Xiao, D. Liu, and J. Wang, "Deep high-resolution representation learning for human pose estimation," in *Proceedings of the IEEE/CVF Conference on Computer Vision and Pattern Recognition (CVPR)*, June 2019.
- [56] M. Li, Y.-M. Zhai, Y.-W. Luo, P.-F. Ge, and C.-X. Ren, "Enhanced transport distance for unsupervised domain adaptation," in *Proceedings of the IEEE/CVF Conference on Computer Vision and Pattern Recognition (CVPR)*, June 2020.
- [57] M. Arjovsky, S. Chintala, and L. Bottou, "Wasserstein generative adversarial networks," in *ICML*, 2017.
- [58] Y. Yan, W. Li, H. Wu, H. Min, M. Tan, and Q. Wu, "Semi-supervised optimal transport for heterogeneous domain adaptation," in *IJCAI*, 2018.
- [59] B. B. Damodaran, B. Kellenberger, R. Flamary, D. Tuia, and N. Courty, "Deepjdot: Deep joint distribution optimal transport for unsupervised domain adaptation," in *Proceedings of the European Conference on Computer Vision (ECCV)*, September 2018.
- [60] L. Chen, Y. Zhang, R. Zhang, C. Tao, Z. Gan, H. Zhang, B. Li, D. Shen, C. Chen, and L. Carin, "Improving sequence-to-sequence learning via optimal transport," *ArXiv*, vol. abs/1901.06283, 2019.
- [61] Y.-C. Chen, L. Li, L. Yu, A. E. Kholy, F. Ahmed, Z. Gan, Y. Cheng, and J. Liu, "Uniter: Learning universal image-text representations," *ArXiv*, vol. abs/1909.11740, 2019.
- [62] R. Xu, P. Liu, L. Wang, C. Chen, and J. Wang, "Reliable weighted optimal transport for unsupervised domain adaptation," in *Proceedings of the IEEE/CVF Conference on Computer Vision and Pattern Recognition (CVPR)*, June 2020.
- [63] S. Yuan, K. Bai, L. Chen, Y. zhe Zhang, C. Tao, C. Li, G. Wang, R. Henao, and L. Carin, "Weakly supervised cross-domain alignment with optimal transport," *ArXiv*, vol. abs/2008.06597, 2020.
- [64] J. Lee, M. Dabagia, E. L. Dyer, and C. Rozell, "Hierarchical optimal transport for multimodal distribution alignment," in *NeurIPS*, 2019.
- [65] D. Bahdanau, K. Cho, and Y. Bengio, "Neural machine translation by jointly learning to align and translate," *CoRR*, vol. abs/1409.0473, 2015.
- [66] J. Gehring, M. Auli, D. Grangier, and Y. Dauphin, "A convolutional encoder model for neural machine translation," in *ACL*, 2017.
- [67] X. Wang, X. He, Y. Cao, M. Liu, and T.-S. Chua, "Kgat: Knowledge graph attention network for recommendation," *Proceedings of the 25th ACM SIGKDD International Conference on Knowledge Discovery & Data Mining*, 2019.
- [68] Q. Wu, H. Zhang, X. Gao, P. He, P. Weng, H. Gao, and G. Chen, "Dual graph attention networks for deep latent representation of multifaceted social effects in recommender systems," *The World Wide Web Conference*, 2019.

- [69] L. Bao, B. Ma, H. Chang, and X. Chen, "Masked graph attention network for person re-identification," *2019 IEEE/CVF Conference on Computer Vision and Pattern Recognition Workshops (CVPRW)*, pp. 1496–1505, 2019.
- [70] L. Li, Z. Gan, Y. Cheng, and J. Liu, "Relation-aware graph attention network for visual question answering," *2019 IEEE/CVF International Conference on Computer Vision (ICCV)*, pp. 10 312–10 321, 2019.
- [71] J. Liu, Z. Zha, R. Hong, M. Wang, and Y. Zhang, "Deep adversarial graph attention convolution network for text-based person search," *Proceedings of the 27th ACM International Conference on Multimedia*, 2019.
- [72] Z. Zhang, Y. Xie, D. Li, W. Zhang, and Q. Tian, "Learning to align via wasserstein for person re-identification," *IEEE Transactions on Image Processing*, vol. 29, pp. 7104–7116, 2020.
- [73] J. Li, S. Zhang, Q. Tian, M. Wang, and W. Gao, "Pose-guided representation learning for person re-identification," *IEEE transactions on pattern analysis and machine intelligence*, 2019.
- [74] L. Wei, S. Zhang, H. Yao, W. Gao, and Q. Tian, "Glad: Global-local-alignment descriptor for pedestrian retrieval," *Proceedings of the 25th ACM international conference on Multimedia*, 2017.
- [75] M. Ye, J. Shen, X. Zhang, P. Yuen, and S.-F. Chang, "Augmentation invariant and instance spreading feature for softmax embedding," *IEEE transactions on pattern analysis and machine intelligence*, vol. PP, 2020.
- [76] D. Li, X. Wei, X. Hong, and Y. Gong, "Infrared-visible cross-modal person re-identification with an x modality," in *AAAI*, 2020.
- [77] J. Shen, Y. Qu, W. Zhang, and Y. Yu, "Wasserstein distance guided representation learning for domain adaptation," in *AAAI*, 2018.
- [78] G. Peyré and M. Cuturi, "Computational optimal transport," *Found. Trends Mach. Learn.*, vol. 11, pp. 355–607, 2019.
- [79] G. Peyré, M. Cuturi, and J. Solomon, "Gromov-wasserstein averaging of kernel and distance matrices," in *ICML*, 2016.
- [80] R. Hadsell, S. Chopra, and Y. LeCun, "Dimensionality reduction by learning an invariant mapping," *2006 IEEE Computer Society Conference on Computer Vision and Pattern Recognition (CVPR'06)*, vol. 2, pp. 1735–1742, 2006.
- [81] M. Xu, H. Wang, B. Ni, Q. Tian, and W. Zhang, "Cross-domain detection via graph-induced prototype alignment," *2020 IEEE/CVF Conference on Computer Vision and Pattern Recognition (CVPR)*, pp. 12 352–12 361, 2020.
- [82] X. Yang, C. Deng, T. Liu, and D. Tao, "Heterogeneous graph attention network for unsupervised multiple-target domain adaptation," *IEEE transactions on pattern analysis and machine intelligence*, vol. PP, 2020.
- [83] P. Wang, Z. Zhao, F. Su, Y. Zhao, H. Wang, L. Yang, and Y. Li, "Deep multi-patch matching network for visible thermal person re-identification," *IEEE Transactions on Multimedia*, pp. 1–1, 2020.
- [84] W. Yang, H. Huang, Z. Zhang, X. Chen, K. Huang, and S. Zhang, "Towards rich feature discovery with class activation maps augmentation for person re-identification," in *Proceedings of the IEEE/CVF Conference on Computer Vision and Pattern Recognition (CVPR)*, June 2019.
- [85] N. Dalal and B. Triggs, "Histograms of oriented gradients for human detection," in *2005 IEEE computer society conference on computer vision and pattern recognition (CVPR'05)*, vol. 1. IEEE, 2005, pp. 886–893.
- [86] S. Liao, Y. Hu, X. Zhu, and S. Z. Li, "Person re-identification by local maximal occurrence representation and metric learning," in *Proceedings of the IEEE conference on computer vision and pattern recognition*, 2015, pp. 2197–2206.
- [87] K. He, X. Zhang, S. Ren, and J. Sun, "Deep residual learning for image recognition," in *Proceedings of the IEEE Conference on Computer Vision and Pattern Recognition (CVPR)*, June 2016.
- [88] J. Deng, W. Dong, R. Socher, L. Li, K. Li, and L. Fei-Fei, "Imagenet: A large-scale hierarchical image database," in *CVPR*, 2009.
- [89] T.-Y. Lin, M. Maire, S. Belongie, J. Hays, P. Perona, D. Ramanan, P. Dollár, and C. L. Zitnick, "Microsoft coco: Common objects in context," *ArXiv*, vol. abs/1405.0312, 2014.
- [90] G. Wang, S. Yang, H. Liu, Z. Wang, Y. Yang, S. Wang, G. Yu, E. Zhou, and J. Sun, "High-order information matters: Learning relation and topology for occluded person re-identification," in *Proceedings of the IEEE/CVF Conference on Computer Vision and Pattern Recognition (CVPR)*, June 2020.
- [91] L. V. D. Maaten and G. E. Hinton, "Visualizing data using t-sne," *Journal of Machine Learning Research*, vol. 9, pp. 2579–2605, 2008.